PHYSICAL REVIEW B **105**, 184421 (2022)

Magnetism and spin transport at permalloy/Cu$_{1-x}$Tb$_x$ interfaces

Sheng Jiang,[1,2,4,*] Zhaocong Huang,[1,*] Qi An,[3] Wen Zhang,[2] Yuli Yin,[1] Dong Zhang,[1] Jun Du,[5] Biao You,[5]
Jian-Guo Zheng,[6] Wenqing Liu,[3,†] and Ya Zhai[1,5,‡]
[1]*School of Physics, Southeast University, Nanjing 211189, Jiangsu, China*
[2]*School of Microelectronics, Northwestern Polytechnical University, Xi'an 710072, Shaanxi, China*
[3]*Department of Electronic Engineering, Royal Holloway University of London, Egham TW20 0EX, United Kingdom*
[4]*Yangtze River Delta Research Institute of NPU, Taicang 215400, Jiangsu, China*
[5]*National Laboratory of Solid-State Microstructures, Nanjing University, Nanjing 210093, Jiangsu, China*
[6]*Irvine Materials Research Institute, University of California, Irvine, California 92697-2800, USA*

(Received 22 August 2021; revised 23 February 2022; accepted 9 May 2022; published 20 May 2022)

The significance of spin transport over an interface in energy-efficient spintronic devices has stimulated interest in the spintronic society during the last few decades. Here, interfaces of permalloy/Cu$_{1-x}$Tb$_x$ (Py/Cu-Tb) were investigated in depth. As the Cu-Tb thickness increases, we found that the saturation magnetization of the bilayers falls and then plateaus. Element-specific x-ray magnetic circular dichroism studies suggest that the Tb moment aligns opposite to the Fe and Ni moments, forming a self-assembled antiferromagnetic interface. As a result, the Cu-Tb adjacent layer to Py and the interface have a significant impact on spin transport. Relevant parameters, such as spin mixing conductance, spin diffusion length, and damping, can be tuned by inserting a thin Cu layer between Py and Tb or varying the compositions of Cu-Tb alloys. Using rare-earth Tb, we provide an effective method for controlling the spin transport and magnetism of ferromagnet/normal-metal interfaces. This approach is expected to have a great deal of potential in spintronic applications.

DOI: 10.1103/PhysRevB.105.184421

I. INTRODUCTION

Efficiently generating and transmitting spin currents is critical for applications in novel spintronic devices. For instance, generated spin current can be utilized as a torque [1,2] to switch magnetization or maintain a steady magnetic precession. This mechanism of spin-transfer torque (STT) has been applied to STT magnetic random access memory [3,4] and STT nano-oscillators [5,6]. In general, there are several ways to generate spin currents: (1) spin-polarized currents, which use the exchange interaction between conduction electrons and local spins in magnets [7], and (2) pure spin currents, which use spin-orbit interaction, such as spin pumping effect [8], spin Hall effect [9], Rashba-Edelstein effect [10], and spin Seebeck effect [11]. The interface is key for the capability of generating and transmitting highly efficient spin currents, which, in turn, can tailor magnetic dynamics [7,11,12]. It thus expands the scope of spintronics applications [13,14]. To effectively utilize the spin currents, one has to minimize the loss of spin currents during the transport. Therefore, interfaces with low spin memory loss (SML) [11] and high spin transparency [15] are required for highly efficient spin current transportation. Heavy metals (HMs), such as Pt, Pd, W, and Ta, have strong spin-orbit couplings, making them suitable for spin generation and transportation. Interfacial engineering of ferromagnet/heavy metal (FM/HM) has thus received a lot of attention [16–18]. Recently, both theoretical [19] and experimental [20] studies suggest that antiferromagnetic (AFM) materials (IrMn, PtMn, and so on) show large spin-orbit torque and spin Hall angle [21]. Spins can pass through AFM layers as well. Rare-earth (RE) materials, on the other hand, are known to have a strong spin-orbit coupling as well and tend to pair antiferromagnetically with transition metals and their alloys, forming ferrimagnets [21–24]. Similarly, the RE magnetic moment in FM/RE bilayers could self-assemble to be antiferromagnetically coupled with FM near the interface, forming an AFM monolayer [25–29]. So far, the magnetism and spin transport at such FM/RE interfaces have yet to be thoroughly investigated.

In this paper, we investigate magnetism and spin dynamics of permalloy/Cu$_{1-x}$Tb$_x$ (Py/Cu-Tb) films, where the moments of Py and Tb exhibit AFM interaction on interfaces, as evidenced by x-ray magnetic circular dichroism (XMCD) and vibrating sample magnetometer (VSM) results. For the Py/Tb films with $x = 100\%$, we observe their damping values show strong dependencies on the Py and Tb thicknesses. Furthermore, by inserting a thin Cu layer between Py and Tb, the magnetism and spin dynamics can be effectively tuned. The Cu insertion layer reduces the damping enhancement in Py/Tb, implying that Cu destroys the interfacial AFM coupling. In addition, we found the compositions of Tb in the Cu-Tb alloys can be used to tune not only the damping but also the spin transport parameters such as spin diffusion length and spin mixing conductance. We, therefore, provide an

---

[*] These authors contributed equally to this work.

[†] Corresponding author: Wenqing.Liu@rhul.ac.uk

[‡] Corresponding author: yazhai@seu.edu.cn

effective way toward tuning the magnetism and spin transport in FM/normal metal (NM) bilayers.

II. MATERIALS AND METHODS

The multilayer films, consisting of Ta(5 nm)/Py(d_{Py})/Cu(d_{Cu})/$\mathrm{Cu}_{1-x}\mathrm{Tb}_x$($d_{\mathrm{Cu-Tb}}$)/Ta(2 nm) with varying layer thicknesses and $\mathrm{Cu}_{1-x}\mathrm{Tb}_x$ compositions, were deposited by magnetron sputtering on silicon substrates. The 5- and 2-nm Ta layers serve as buffer and capping layers, respectively. During the deposition, Ar pressure is 0.5 Pa and the DC power is 30 W, and a 5-mT magnetic field was applied to induce a small in-plane uniaxial anisotropy. Cu-Tb alloys were sputtered from a Cu target with Tb chips located symmetrically in a ring on top of the Cu target, except for the Tb layer ($x = 100\%$), which was sputtered from a pure Tb target. The Tb concentration x was adjusted by varying the number of Tb chips.

The compositions of the films were determined by energy-dispersive x-ray diffraction spectroscopy, and the structures were investigated by x-ray diffraction (XRD) and transmission electron microscopy (TEM). The measurements of magnetostatic properties were carried out by the VSM technique. X-ray absorption spectroscopy (XAS) and XMCD at the Fe $L_{2,3}$, the Ni $L_{2,3}$, and the Tb $M_{4,5}$ absorption edges were performed on beamline I10 at the Diamond Light Source, UK. Circularly polarized x rays with 100% degree of polarization were used to resolve XMCD signals from each of the magnetic elements. The light helicity was switched in a saturating magnetic field of 6 T, which was applied in normal incidence to the film plane and parallel to the beam. Total electron yield (TEY) and total fluorescence yield (TFY) were detected. The magnetodynamic properties were investigated using a cavity ferromagnetic resonance (FMR) technique at a fixed frequency of 9.78 GHz, with the angle between the field and the sample surface normal (θ_{H}) ranging 0–90°. All of the measurements were performed at room temperature.

III. RESULTS AND DISCUSSION

A. Structure and static magnetic properties

In Fig. 1(a), the XRD spectra of Py(10 nm)/$\mathrm{Cu}_{1-x}\mathrm{Tb}_x$(32 nm) films with $0 < x \leqslant 100\%$ shows clear crystalline diffraction peaks of Py(111) texture, except for $x = 2\%$ where a Cu (111) peak is presented. The Tb peak only appears at pure Tb ($x = 100\%$). The disappearance of the Cu (111) peak for $x > 5\%$ could be due to the signal being too weak to be detected, or attributed to the Cu-Tb alloy undergoing a transition from a polycrystalline to an amorphous phase. The cross-section TEM image of Py(10 nm)/$\mathrm{Cu}_{1-x}\mathrm{Tb}_x$(32 nm) film with $x = 22\%$ in Fig. 1(b) confirms that the Cu-Tb alloy turns to amorphous when $x = 22\%$ and the structure of Py remains polycrystalline. In addition, it shows clear interfaces of Ta/Py and Py/Cu-Tb, and the interfacial alloying or diffusion seems negligibly small (<1 nm roughness at the Py/Cu-Tb interface).

In-plane magnetic hysteresis loops were measured by applying a magnetic field perpendicular (hard axis) and parallel (easy axis) to the direction of the induced uniaxial anisotropy by the 5-mT field, as shown in the typical hysteresis loops of Py (10 nm)/Tb (4 nm) plotted in the inset of Fig. 1(c). From the hysteresis loops, the saturation magnetizations (M_{S}) with different thicknesses of the Tb layer are extracted and presented in Fig. 1(c). In Fig. 1(c), we see that M_{S} decreases with increasing Tb ($x = 100\%$) thickness from 820 emu/cm^3 ($d_{\mathrm{Tb}} = 1$ nm) to 650 emu/cm^3 ($d_{\mathrm{Tb}} = 16$ nm), and then remains at the same value at $d_{\mathrm{Tb}} = 32$ nm, which implies that a Tb magnetic moment near the interface might be induced by the Py layer and is antiparallel to that of Py. Figure 1(d) shows the trends of M_{S} with different thicknesses of Cu-Tb layers upon dilution of Tb from Cu. As the Tb concentration decreases, the magnetitude of M_{S} variation becomes weaker, and finally, M_{S} does not change obviously for $x = 0\%$ (pure Cu) in Fig. 1(d). This indicates that the Tb atoms play a key role in the decrease of the total magnetization of thin films, which is further proven in Fig. 1(e). By inserting a Cu layer between Py and Tb, we find that 1-nm-thick Cu can largely destroy this Ms decrease and a 4-nm-thick Cu interlayer totally surpresses this decrease. These observations suggest that the decrease of M_{S} could be due to the direct AFM coupling of Py and Tb. More specifically, one possible minor contribution is the interfacial Py-Tb alloying which forms a ferrimagnet, while another possible contribution is the magnetic proximity effect that orders the Tb moments in the vicinity of the interface, where the Tb atoms are antiferromagnetically coupled to Py [27,28].

To better understand the mechanism behind the M_{S} variation in Py/Cu-Tb films, we performed element-specific XAS/XMCD measurements, which are effective tools for analyzing the magnetic moment of one particular element [30,31]. The measurements were carried out at the Fe (Ni) $L_{2,3}$ and Tb $M_{4,5}$ absorption edges, with application of a 6-T magnetic field at room temperature. Figure 2 shows the spectra of the Py(10 nm)/Tb(4 nm) and Py(10 nm)/Cu(1 nm)/Tb(4 nm) thin films, which are similar to those in previous studies [30,31]. The XMCD was obtained by taking the difference of the XAS at right (I^+) and left (I^-) circularly polarized x rays, achieved by flipping the x-ray helicity. The XMCD signals of Tb [Fig. 2(c)] and Fe (Ni) [Figs. 2(a) and 2(b)] are opposite, thus indicating the AFM nature of the Py/Tb bilayers [32]. Similar behavior is observed when a 1-nm-thick Cu is inserted between the Py and Tb layers in Figs. 2(d). The Curie temperature of bulk Tb is lower than room temperature, and thus the weak XMCD signal here should be induced by the Py layer. For thicker Cu insertion layers ($d_{\mathrm{Cu}} = 2$ and 4 nm), we did not obtain a detectable XMCD signal of Tb, which could be due to the signal being too weak to be detected or the breaking of Py/Tb AFM coupling. According to the sum rules [33,34], we calculate the spin moments $m_S = 2.2\mu_{\mathrm{B}}$ $(0.7\mu_{\mathrm{B}})$ and orbital moments $m_L = 0.2\mu_{\mathrm{B}}$ $(0.1\mu_{\mathrm{B}})$ for Fe (Ni) atoms which is consistent with the literature [35,36].

B. Dynamic magnetic properties

After confirming the AFM coupling on the Py/Tb interface, we start to study the mangetodynamics of Py/Cu-Tb films. We first study the effect of the Py/Tb ($x = 100\%$) interface. Figure 3(a) shows the representative FMR spectra of Py (10 nm)/Tb (2 nm) with different out-of-plane angle θ_H. Resonance fields H_{res}, extracted from FMR spectra, are plotted as a function of θ_H with respect to the z axis in

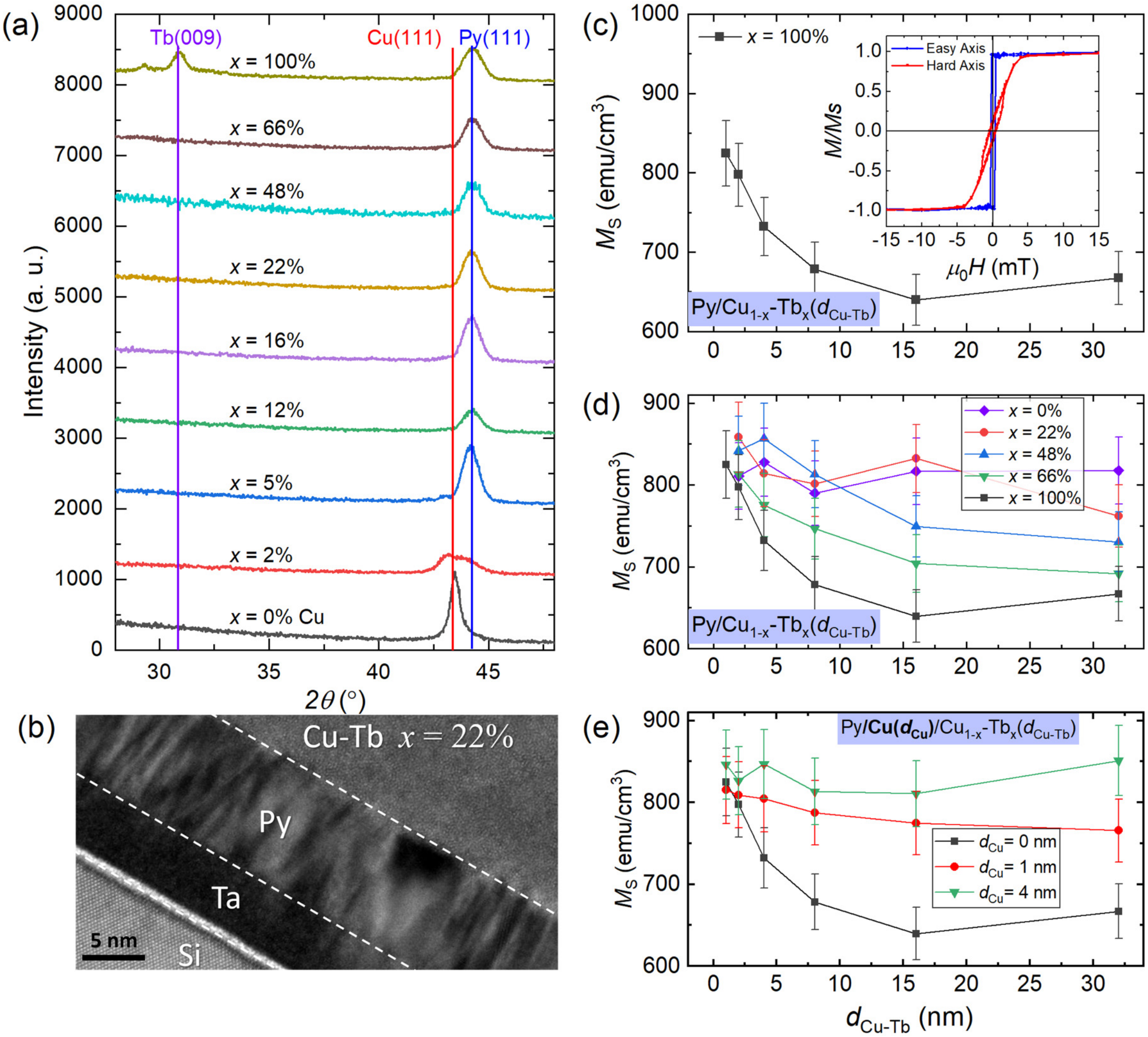

FIG. 1. (a) XRD curves for Py(10 nm)/Cu$_{1-x}$Tb$_x$(32 nm) films, with the Tb composition $x = 2\%$, 5%, 12%, 16%, 22%, 48%, 66%, and 100%, respectively. A 32-nm-thick Cu film on a silicon substrate is used as a reference sample. (b) TEM image of Py(10 nm)/Cu$_{1-x}$Tb$_x$(32 nm) film with $x = 22\%$. Thickness dependence of saturation magnetization M_S for (c) Py/Cu-Tb bilayer ($x = 100\%$), (d) Py/Cu-Tb bilayer with different Tb compositions, and (e) Py/Cu/Cu-Tb trilayer ($x = 100\%$). The inset in (c) is typical hysteresis loops of Py (10 nm)/Tb (4 nm) by applying the magnetic field perpendicular (hard axis) and parallel (easy axis) to the direction of the induced uniaxial anisotropy in the film plane.

Fig. 3(b). It shows a minimum at $\theta_H = 90^\circ$—that is, the field is applied in the film plane—and reaches a maximum at $\theta_H = 0^\circ$, which is expected for the Py film with easy in-plane anisotropy. The peak-to-peak linewidth ΔH is also extracted in Fig. 3(c). By analyzing the H_{res} and ΔH, we extract the magnetization dynamic damping and other relevant parameters.

It is known that the magnetization dynamics can be described by the Landau-Lifshitz-Gilbert (LLG) equation

$$\frac{d\boldsymbol{M}}{dt} = -\gamma \boldsymbol{M} \times \boldsymbol{H}_{\mathrm{eff}} + \frac{\alpha}{M_S}\boldsymbol{M} \times \frac{d\boldsymbol{M}}{dt}. \tag{1}$$

The first term is the magnetization precession torque, and the second term is the damping torque. $\boldsymbol{H}_{\mathrm{eff}}$ is the effective field, α is the damping constant. γ is the gyromagnetic ratio, $\boldsymbol{M}$ is the magnetization vector, and M_S is the saturation magnetization. To fit the experimental data of FMR linewidth, we first need to fit the data of the angular dependence of H_{res}. The free energy density of a polycrystalline film system is given as

$$\begin{aligned} F = & -M_S H[\cos\theta \cos\theta_{\mathrm{H}} + \sin\theta \sin\theta_{\mathrm{H}}] \\ & + 2\pi M_S^2 \cos^2\theta - K_\perp \cos^2\theta + K_u \cos^2\theta, \end{aligned} \tag{2}$$

where θ and θ_{H} are the angle of the magnetization vector and applied field with respect to the film normal, respectively [see the inset of Fig. 3(b)]. The first term is the Zeeman energy, the second term is the demagnetizing energy, the third term represents the second-order surface perpendicular anisotropy energy, and the fourth term stands for in-plane uniaxial anisotropy energy. By minimizing the free energy density,

$$\frac{\partial F}{\partial \theta} = H \sin(\theta - \theta_{\mathrm{H}}) - 4\pi M_{\mathrm{eff}} \sin(2\theta) = 0, \tag{3}$$

and then solving the LLG equation, the dispersion relation for the resonance field H_{res} as a function of field orientation θ_{H} is

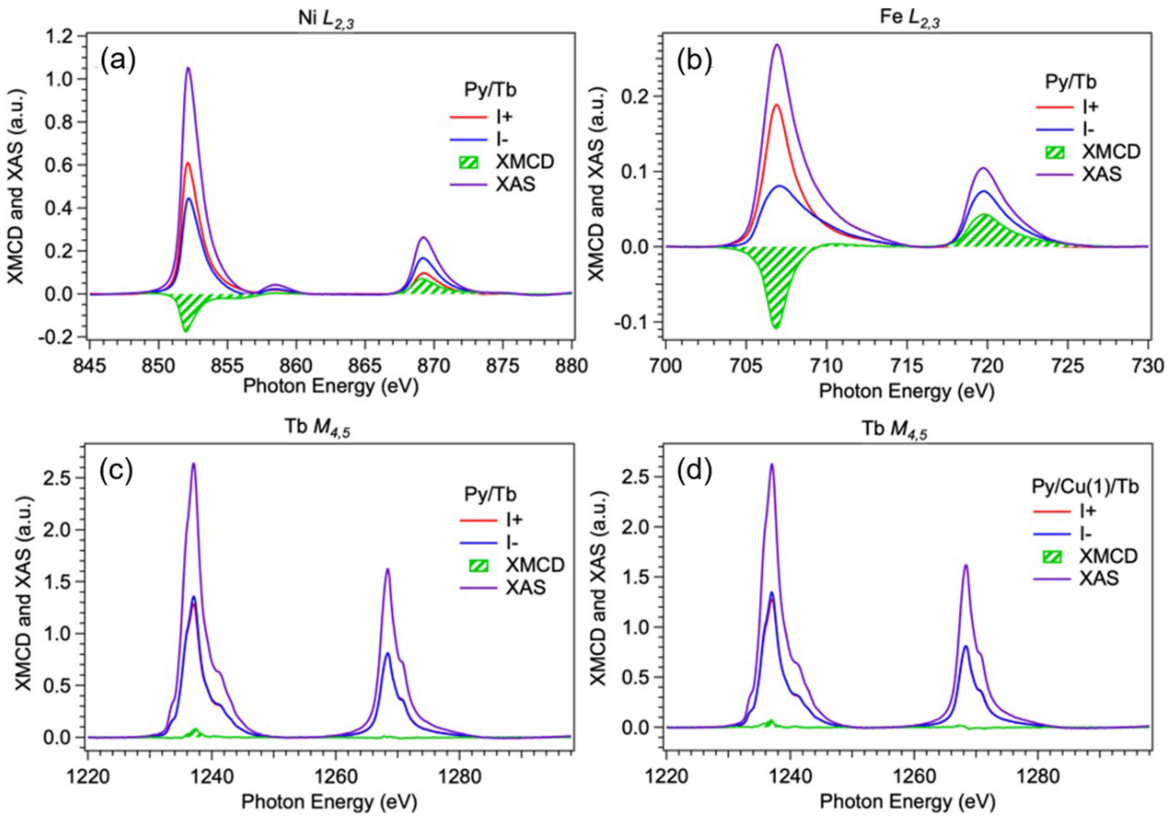

FIG. 2. XAS and XMCD spectra for (a) Ni $L_{2,3}$ edges, (b) Fe $L_{2,3}$ edges, and (c) Tb $M_{4,5}$ edges in the Py (10 nm)/Tb (4 nm) film. For comparison, (d) Tb $M_{4,5}$ edges in the Py (10 nm)/Cu (1 nm)/Tb (4 nm) film are also shown.

obtained,

$$f = \frac{\gamma}{2\pi}\sqrt{[H\cos(\theta-\theta_{\mathrm{H}}) - 4\pi M_{\mathrm{eff}}\cos(2\theta)] \times [H\cos(\theta-\theta_H) - 4\pi M_{\mathrm{eff}}\cos^2\theta]}, \tag{4}$$

where $4\pi M_{\mathrm{eff}} = 4\pi M_S - H_K$ is the effective magnetization, $H_K = \frac{2K_\perp - 2K_u}{M_S}$ represents the magnetic anisotropy field. $f = 9.78$ GHz is the frequency of microwave. H refers to the resonance field H_{res}. Using Eqs. (3) and (4) to fit the experimental data (H_{res} as a function of θ_{H}) in Fig. 3(b), we are able to extract the free parameters of $4\pi M_{\mathrm{eff}}$, γ, and θ. Here, θ is a function of θ_{H}.

The FMR linewidth ΔH mainly consists of intrinsic Gilbert contribution ΔH_{G}, spin pumping ΔH_{SP} [12], inhomogeneous $\Delta H_{\mathrm{inhom}}$ [29], and two-magnon scattering ΔH_{TMS} [30], i.e.,

$$\Delta H = \Delta H_{\mathrm{G}} + \Delta H_{\mathrm{SP}} + \Delta H_{\mathrm{inhom}} + \Delta H_{\mathrm{TMS}}. \tag{5}$$

Both Gilbert and spin pumping contributions have the same angular dependencies on applied fields, which we define as $\Delta H_\alpha = \Delta H_{\mathrm{G}} + \Delta H_{\mathrm{SP}}$. Then ΔH_α can be determined by the following equation [31]:

$$\Delta H_\alpha = \frac{\gamma\alpha}{\sqrt{3}M_S}\frac{dH}{d\omega}F_{\theta\theta}, \tag{6}$$

where ω is the microwave frequency. $F_{\theta\theta}$ is the second partial derivatives of the free energy density F. The inhomogeneous linewidth $\Delta H_{\mathrm{inhom}}$ consists of two components,

$$\begin{aligned}\Delta H_{\mathrm{inhom}} &= \Delta \mathrm{H}^{\theta}_{\mathrm{inhom}} + \Delta \mathrm{H}^{\mathrm{M}}_{\mathrm{inhom}} \\ &= \left|\frac{\partial H}{\partial \theta_H}\right|\Delta\theta_H + \left|\frac{\partial H}{\partial 4\pi M_{\mathrm{eff}}}\right|\Delta 4\pi M_{\mathrm{eff}}\end{aligned} \tag{7}$$

where $\Delta\theta_H$ is the spread in the orientations of the magnetization mostly due to the inhomogeneity of the FM thin film, and $\Delta 4\pi M_{\mathrm{eff}}$ represents the magnitude of the inhomogeneity of the local demagnetizing field. In our case, the interfacial Tb moments could cause fluctuating internal magnetic fields acting on the adjacent Py layer, which could also contribute to this inhomogeneous broadening. As for the contribution of two-magnon scattering ΔH_{TMS}, it is known to disappear at perpendicular fields ($\theta_H = 0^\circ$) [30]. If there exists a significant two-magnon scattering, the total linewidth should show $\Delta H(\theta_H = 0^\circ) < \Delta H(\theta_H = 90^\circ)$. In Fig. 3(c), the total linewidth $\Delta H(\theta_H = 0^\circ) \approx \Delta H(\theta_H = 90^\circ)$, so we claim that the two-magnon scattering is negligible as well in our samples. Equations (1)–(7) can be used to fit the angular dependencies of H_{res} and ΔH. Detailed methods can also be found in Refs. [24,35]. As shown in Fig. 3(c), in the various contributions to an extracted linewidth, we found that the $\Delta H_{\mathrm{inhom}}$ is negligible in comparison with

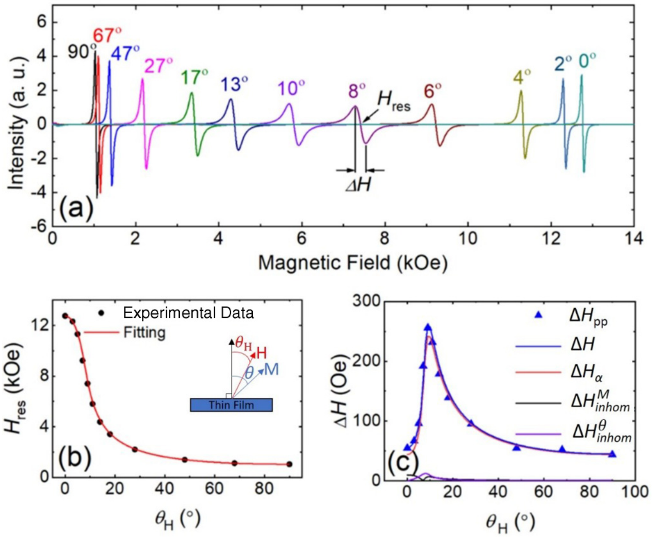

FIG. 3. (a) FMR spectra of Py (10 nm)/Tb (2 nm) at at 9.78 GHz, with the sample rotating from in-plane ($\theta_H = 90^\circ$) to the normal direction ($\theta_H = 0^\circ$). (b) Resonance field as a function of out-of-plane angle θ_H extracted from the FMR spectra. The dots are experimental results, and the solid line is the fitting result. (d) FMR linewidth as a function of θ_H. The solid lines are fitting results with different contributions.

$\Delta H_\alpha = \Delta H_G + \Delta H_{SP}$, in agreement with other studies [33], indicating the excellent homogeneity of Py film. Consequently, the damping $\alpha = \alpha_G + \alpha_{SP}$ resulting from Gilbert and spin pumping linewidth can then be determined.

To investigate the effect of the Tb layer on the magnetic dynamics of the system, we conducted FMR measurements. Figure 4(a) shows the in-plane ($\theta_H = 90^\circ$) FMR spectra of Py (10 nm)/Tb(d_{Tb}) with various Tb thicknesses. Peak-to-peak FMR linewidth, ΔH, increases dramatically by one order of magnitude, from 41 Oe ($d_{\mathrm{Tb}} = 0$) to 475 Oe ($d_{\mathrm{Tb}} = 16\,\mathrm{nm}$), implying a dramatic damping enhancement. Note that the resonance fields also vary with the Tb thickness in Fig. 4(a), which could be caused by the following reasons: (1) the AFM coupling probably generates effective fields from the ordered Tb layer; (2) the in-plane magnetic anisotropy varies as Tb thickness increases, which contributes to the shifts; (3) a perpendicular magnetic anisotropy field of the Py/Tb bilayer could exist as it is known that FM/RE multilayers can exhibit PMA. To figure out the reason causing this giant enhancement in damping, we extract the angular dependent FMR linewidths for different d_{Tb} and d_{Py}, respectively, as shown in Figs. 4(b) and 4(d). The linewidths were again fitted by using Eqs. (1)–(7), and the damping constant of the Py/Tb bilayers with varying thicknesses of d_{Tb} and d_{Py} was extracted, which increases from 0.0083 ($d_{\mathrm{Tb}} = 0$) to 0.10 ($d_{\mathrm{Tb}} = 8\,\mathrm{nm}$) before stabilizing at 0.118 ($d_{\mathrm{Tb}} > 8\,\mathrm{nm}$). We, here, define a variable $4\pi M_S \alpha_G$ and plot it in Figs. 4(c) and 4(e) for the convenience of fits later on. By inserting a Cu layer between Py and Tb, we observe a similar damping rise followed by saturation at some points. On the other hand, increasing the Cu insertion thickness reduces the amplitude of this damping enhancement. Finally, with a 4-nm Cu insertion layer, the damping shows a weak d_{Tb} dependence.

We try to explain the damping behavior with the spin pumping theory. As we mentioned, the extracted damping $\alpha = \alpha_G + \alpha_{SP}$ results from intrinsic Gilbert and spin pumping linewidths. The spin pumping effect is known as one of the main sources of the damping increase for FM/NM bilayers. Based on the spin pumping theory, spin-polarized current is generated by FMR, and then crosses the Py/Tb interface and diffuses into the Tb layer. When it reaches the next interface, the reflection will occur, and the reflected spin current will partially counteract the pumped spin current. The thicker the Tb layer, the weaker the reflected spin current, and the stronger the pumped spin current. However, when the Tb layer thickness exceeds the spin diffusion length λ_{SD}, the spin current is relaxed before reaching the next interface. The effective spin mixing conductance is also known to be influenced by both the SML at the interface and the momentum loss in the NM layer. The SML occurs at the interface, causing the damping to increase. Using spin pumping and SML theory, the phenomenological expression of the overall damping can be given as [34]

$$\alpha = \alpha_{\mathrm{G}} + \alpha_{\mathrm{SP}} = \alpha_{\mathrm{G}} + \frac{g\mu_B g_{\mathrm{eff}}^{\uparrow\downarrow}}{4\pi M_S d_{\mathrm{FM}}}\{\Delta + (1-\Delta) \times \left[1 - (1-\Delta)e^{\frac{-2(d_{\mathrm{NM}}-d_{\mathrm{int}})}{\lambda_{\mathrm{SD}}}}\right]\Big\}, \tag{8}$$

where $g = 2.1$, $\mu_{\mathrm{B}} = 9.274 \times 10^{-21}$ erg/G is Bohr magnetron, M_{S} is measured by VSM (see Fig. 1), $g_{\mathrm{eff}}^{\uparrow\downarrow}$ is the interface effective spin mixing conductance, and λ_{SD} stands for the spin diffusion length of the NM layer. d_{FM} and d_{NM} represent the thickness of Py and Tb layers, respectively. Δ is the SML-induced damping increase, representing the percentage of spin current loss at the Py/Cu-Tb interface. $\Delta = 0$ means that the SML at the interface is negligible. d_{int} is the parameter indicating the thickness of the interfacial roughness. The possible interfacial alloy at the interface leads to a decrease in the effective thickness of the Cu-Tb layers. The first term in Eq. (8) is the Gilbert damping $\alpha_{\mathrm{G}} = 0.0083$, including the contribution of the Ta seed layer. The second term is the damping enhancement due to the spin momentum absorbed in the NM layer.

We perform a two-step fit for the Py/Tb data as there are two sets of results with different Tb and Py thicknesses in Figs. 4(c) and 4(e), respectively. It is also worth noting that the M_S is dependent on the thickness of both Py and Cu-Tb. The equation can be rewritten to include the measured M_S as

$$4\pi M_S \alpha_{\mathrm{SP}} = g\mu_B g_{\mathrm{eff}}^{\uparrow\downarrow}\{\Delta + (1-\Delta) \times \left[1 - (1-\Delta)e^{\frac{-2(d_{\mathrm{NM}}-d_{\mathrm{int}})}{\lambda_{\mathrm{SD}}}}\right]\Big\}\frac{1}{d_{\mathrm{FM}}}. \tag{9}$$

First, $4\pi M_S \alpha_{\mathrm{SP}}$ is inversely proportional to the d_{FM}. The experimental data in Fig. 4(e) can be first fitted to obtain the slope $S = g\mu_B g_{\mathrm{eff}}^{\uparrow\downarrow}\{\Delta + (1-\Delta)[1 - (1-\Delta)e^{\frac{-2(d_{\mathrm{NM}}-d_{\mathrm{int}})}{\lambda_{\mathrm{SD}}}}]\}$, where $d_{\mathrm{NM}} = 4$ nm. Then, the slope can be implemented into Eq. (9) for fitting the data in Fig. 4(c). The blue solid lines in Figs. 4(c) and 4(e) show the fitting result using Eq. (9). We can determine the $g_{\mathrm{Py/Tb}}^{\uparrow\downarrow} = (4.8 \pm 0.4) \times 10^{16}\ \mathrm{cm}^{-2}$, $\lambda_{\mathrm{SD}} = 12 \pm 2$ nm, $d_{\mathrm{int}} = 1.0 \pm 0.3$ nm, and $\Delta = 3.9 \pm 0.6\%$. The thickness of the interfacial roughness is about 1.0 nm, which

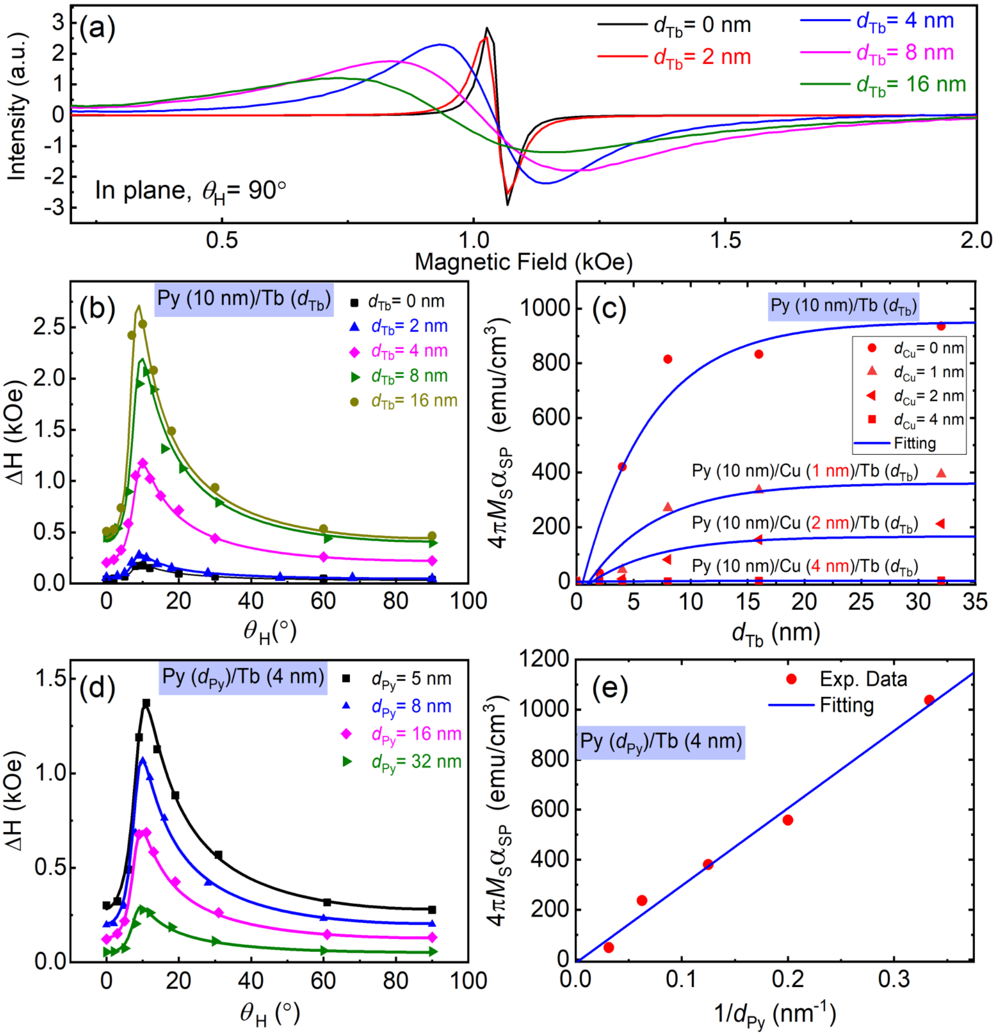

FIG. 4. (a) In-plane FMR spectra of Ta (5 nm)/Py (10 nm)/Tb (d_{Tb})/Ta (2 nm) with $d_{\mathrm{Tb}} = 0$–16 nm. (b) (d) Out-of-plane angular dependence of linewidths ΔH with various Tb thicknesses (0–16 nm) and Py thicknesses (3–32 nm), respectively. (c) $4\pi M_S\alpha_{\mathrm{SP}}$ as a function of Tb thickness with inserting Cu layer ($d_{\mathrm{Cu}} = 0, 1, 2, 4$ nm) in Ta (5 nm)/Py (10 nm)/Cu (d_{Cu})/Tb (4 nm)/Ta (2 nm). (e) $4\pi M_S\alpha_{\mathrm{SP}}$ as a function of reciprocal of Py thickness in Ta(5 nm)/Py (10 nm)/Tb (d_{Tb})/Ta(2 nm). The dots are experimental data and the solid lines are fitting results.

is consistent with the results of the TEM image. The SML contributes 3.9% of the degrade of spin currents, thus giving a minor contribution to the damping enhacement. Interestingly, $g^{\uparrow\downarrow}_{\mathrm{Py/Tb}}$ is one order of magnitude larger than that of Pt ($g^{\uparrow\downarrow}_{\mathrm{Py/Pt}} = 0.26 \times 10^{16}$ cm^{-2}) [8] and Pd ($g^{\uparrow\downarrow}_{\mathrm{Py/Pd}} = 0.15 \times 10^{16}$cm^{-2}) [35]. Furthermore, by inserting a Cu layer between Py and Tb, the damping enhancement is dramatically suppressed by increasing the Cu thickness in Fig. 4(c). The effective interfacial spin mixing conductances are considerably reduced from 1.8 $\times 10^{16}$ cm^{-2} to $\sim$0.01 $\times$ 10^{16} cm^{-2} when the Cu spacer increases from 1 to 4 nm. The interfacial alloying thickness d_{int} is less than 1.5 nm, and the SML parameter $\Delta = 3.3 \pm 0.7\%$, $1.1 \pm 0.4\%$, $1.5 \pm 0.5\%$. The fitting results again confirm the importance of the AFM interface.

For spintronic device applications, damping, spin diffusion length, and spin mixing conductance are important factors. It is advantageous to engineer these factors effectively. The adjacent Tb layer has been shown to significantly increase the damping of the FM layer, and the interface between Py and Tb exhibits a high spin mixing conductance. A Cu layer, on the other hand, has a minor effect on the FM magnetism. By alloying these two metals with Cu and Tb, we aim to engineer their magnetic properties. $\mathrm{Cu}_{1-x}\mathrm{Tb}_x$ compositions vary from 22%, 48%, and 66% to 100%. Again, their FMR linewidths were extracted and presented in Fig. 5(a). For Py (10 nm)/Cu-Tb (4 nm), their overall linewidths rise as the Tb composition increases. Similarly, the thickness dependence of the damping was obtained in Fig. 5(b). The damping follows the same trend, with damping increasing as Cu-Tb thickness increases and eventually plateauing. Fitting the damping with Eq. (9) yields the spin mixing conductance and spin diffusion length, as summarized in Table I. We found that $g^{\uparrow\downarrow}_{Py/Cu-\mathrm{Tb}}$ is tailored from 0.4×10^{16} cm^{-2} to 4.8×10^{16} cm^{-2}, and the spin diffusion length λ_{SD} decreases from 19 to 12 nm as x increases. The interfacial alloying thickness d_{int} remains less than 1.5 nm, and the SML parameter Δ ($< 6.2\%$) remains low. The findings imply that the compositions of Cu-Tb alloys can efficiently tune the spin transport properties.

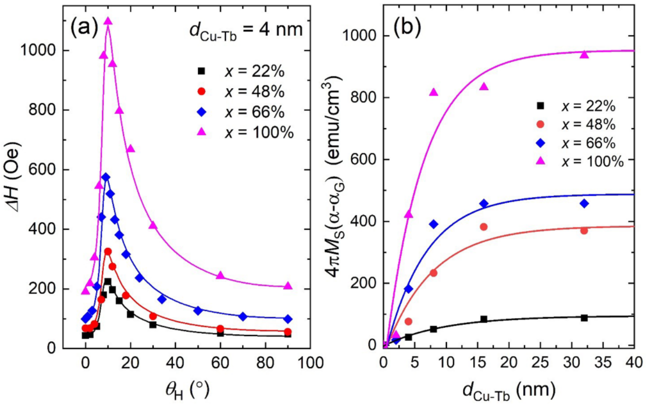

FIG. 5. (a) Out-of-plane angular dependence of the linewidth ΔH in the Py (10 nm)/$\mathrm{Cu}_{1-x}\mathrm{Tb}_x$ (4 nm) thin films. (b) Damping as a function of $\mathrm{Cu}_{1-x}\mathrm{Tb}_x$ thickness with various Tb compositions x.

TABLE I. Spin transport parameters.

x	$g^{\uparrow\downarrow}$ (10^{16} cm^{-2})	λ_{SD} (nm)	d_{int} (nm)	Δ
22%	0.4	19	1.49	6.2%
48%	1.9	15	1.49	5.5%
66%	2.5	13	1.28	5.1%
100%	4.8	12	1.02	3.9%

According to the experimental results, the AFM coupling at the Py/Tb interface plays a vital role in the damping enhancement. At ambient temperature, bulk Tb is a paramagnet; due to the magnetic proximity effect or the possible formation of Fe-Ni-Tb alloys at the interface, the Tb moments are ordered in the area of the interface. The VSM and XMCD results show that the Tb moments are antiparallel to the Ni and Fe moments (i.e., antiferromagnetically coupled). Another effect of the AFM interface is the generation of spin fluctuation at the interface. The spin fluctuation is supposed to increase the spin pumping efficiency [36–38], as the damping is greatly increased while the SML remains low. In addition, the thickness-dependent damping in the Py/Cu-Tb films is due to the degradation of the generated transverse spin current during the spin transport in the Cu-Tb layer. This effect is reflected in the calculated spin diffusion lengths. The spin diffusion length can be further tailored by alloying different materials such as Cu-Tb alloys. The spin mixing conductance is also well engineered.

IV. CONCLUSIONS

In conclusion, we have studied the static and dynamic magnetic properties of Py/Cu-Tb films. Both the XMCD and VSM results provide direct evidence that Py and Tb atoms are antiferromagnetically coupled at the interface. Thanks to this AFM coupling, the damping can be largely tailored by varying the thickness of Py, Cu, and Tb layers as well as the compositions of the Cu-Tb alloys. Using spin pumping theory, we have illustrated the damping increase and extracted the spin mixing conductance and spin diffusion length in Py/Cu-Tb films. Compared to the widely used Py/Pt (Pd), the spin pumping efficiency has been enhanced by one order of magnitude by the interface spin mixing conductance in our Py/Cu-Tb systems. Their spin transport properties, such as spin mixing conductance and spin diffusion length, are engineered effectively by the interfaces. This type of AFM coupling at the interface could be important in generating a massive spin pumping effect, and is expected to stimulate a lot of applications in next-generation AFM spintronics.

ACKNOWLEDGMENTS

This work was supported by the National Key Research and Development Program of China (Grant No. 2017YFA0204800), NSFC (Grants No. 52071079, No. 62104196, and No. 51971109), Basic Research Programs of Taicang (Grant No. TC2021JC19), the Fundamental Research Funds for the Central Universities of China, UK EPSRC (Grant No. EP/S010246/1), Royal Society (Grant No. IEC\ NSFC\ 181680), and Leverhulme Trust (Grant No. LT-SRF1819 \ 15\ 12). Diamond Light Source is acknowledged for the use of beamline I10.

The authors declare that they have no known competing financial interests or personal relationships that could have appeared to influence the work reported in this paper.

---

[1] J. C. Slonczewski, Current-driven excitation of magnetic multilayers, J. Magn. Magn. Mater. **159**, L1 (1996).

[2] L. Berger, Emission of spin waves by a magnetic multilayer traversed by a current, Phys. Rev. B **54**, 9353 (1996).

[3] J. Akerman, Applied physics. toward a universal memory, Science **308**, 508 (2005).

[4] S. Bhatti, R. Sbiaa, A. Hirohata, H. Ohno, S. Fukami, and S. N. Piramanayagam, Spintronics based random access memory: A review, Mater. Today **20**, 530 (2017).

[5] K. Shi, W. Cai, and S. Jiang, Observation of magnetic droplets in magnetic tunnel junctions, Sci. China: Phys., Mech. Astron. **65**, 227511 (2022).

[6] T. Chen, R. K. Dumas, A. Eklund, P. K. Muduli, A. Houshang, A. A. Awad, P. Dürrenfeld, B. G. Malm, A. Rusu, and J. Akerman, Spin-torque and spin-hall nano-oscillators, Proc. IEEE **104**, 1919 (2016).

[7] J. S. Moodera, L. R. Kinder, T. M. Wong, and R. Meservey, Large Magnetoresistance at Room Temperature in Ferromagnetic Thin Film Tunnel Junctions, Phys. Rev. Lett. **74**, 3273 (1995).

[8] Y. Tserkovnyak, A. Brataas, and G. E. W. Bauer, Spin pumping and magnetization dynamics in metallic multilayers, Phys. Rev. B **66**, 224403 (2002).

[9] J. Sinova, S. O. Valenzuela, J. Wunderlich, C. H. Back, and T. Jungwirth, Spin hall effects, Rev. Mod. Phys. **87**, 1213 (2015).

[10] G. Bihlmayer, O. Rader, and R. Winkler, Focus on the rashba effect, New J. Phys. **17**, 050202 (2015).

[11] H. Adachi, K. I. Uchida, E. Saitoh, and S. Maekawa, Theory of the spin seebeck effect, Rep. Prog. Phys. **76**, 036501 (2013).

[12] J. C. Rojas-Sánchez, N. Reyren, P. Laczkowski, W. Savero, J. P. Attané, C. Deranlot, M. Jamet, J. M. George, L. Vila, and H. Jaffrès, Spin Pumping and Inverse Spin Hall Effect in Platinum: The Essential Role of Spin-Memory Loss at Metallic Interfaces, Phys. Rev. Lett. **112**, 106602 (2014).

[13] K. Chen and S. Zhang, Spin Pumping in the Presence of Spin-Orbit Coupling, Phys. Rev. Lett. **114**, 126602 (2015).

[14] Y. Kajiwara, K. Harii, S. Takahashi, J. Ohe, K. Uchida, M. Mizuguchi, H. Umezawa, H. Kawai, K. Ando, K. Takanashi, S. Maekawa, and E. Saitoh, Transmission of electrical signals by spin-wave interconversion in a magnetic insulator, Nature (London) **464**, 262 (2010).

[15] W. Zhang, W. Han, X. Jiang, S.-H. Yang, and S. S. P. Parkin, Role of transparency of platinum–ferromagnet interfaces in determining the intrinsic magnitude of the spin hall effect, Nat. Phys. **11**, 496 (2015).

[16] L. Yang, Y. Fei, K. Zhou, L. Chen, Q. Fu, L. Li, C. Yan, H. Li, Y. Du, and R. Liu, Maximizing spin-orbit torque efficiency of Ta(O)/Py via modulating oxygen-induced interface orbital hybridization, Appl. Phys. Lett. **118**, 032405 (2021).

[17] H. Hayashi, A. Musha, H. Sakimura, and K. Ando, Spin-orbit torques originating from the bulk and interface in Pt-based structures, Phys. Rev. Res. **3**, 013042 (2021).

[18] A. Soumyanarayanan, N. Reyren, A. Fert, and C. Panagopoulos, Emergent phenomena induced by spin-orbit coupling at surfaces and interfaces, Nature (London) **539**, 509 (2016).

[19] R. Cheng, J. Xiao, Q. Niu, and A. Brataas, Spin Pumping and Spin-Transfer Torques in Antiferromagnets, Phys. Rev. Lett. **113**, 057601 (2014).

[20] T. Jungwirth, X. Marti, P. Wadley, and J. Wunderlich, Antiferromagnetic spintronics, Nat. Nanotechnol. **11**, 231 (2016).

[21] S. Fukami, V. O. Lorenz, and O. Gomonay, Antiferromagnetic spintronics, J. Appl. Phys. **128**, 070401 (2020).

[22] J. Finley and L. Liu, Spintronics with compensated ferrimagnets, Appl. Phys. Lett. **116**, 110501 (2020).

[23] D. Zhang, S. Jiang, W. Zhang, C. Luo, Y. Wang, Y. Xu, H. Huang, P. K. J. Wong, Y. Zhai, J. Du, and H. Zhai, The manipulation of magnetization damping in $\mathrm{FeNi}_{1-x}\mathrm{Nd}_x/\mathrm{Cu}/\mathrm{FeCo}_{1-y}\mathrm{Gd}_y$ sandwich structured multilayers, J. Appl. Phys. **117**, 17A716 (2015).

[24] D. Zhang, J. Yue, S. Jiang, Y. Zhai, J. Du, and H. Zhai, Selective tuning of magnetization dynamics damping in Tb- and Nd-doped permalloy ultrathin films by adjacent copper nanolayers, J. Alloys Compd. **672**, 170 (2016).

[25] S. Jiang, L. Sun, Y. Yin, Y. Fu, C. Luo, Y. Zhai, and H. Zhai, Ferromagnetic resonance linewidth and two-magnon scattering in $\mathrm{Fe}_{1-x}\mathrm{Gd}_x$ thin films, AIP Adv. **7**, 056029 (2017).

[26] R. Bläsing, T. Ma, S. H. Yang, C. Garg, F. K. Dejene, A. T. N'Diaye, G. Chen, K. Liu, and S. S. P. Parkin, Exchange coupling torque in ferrimagnetic Co/Gd bilayer maximized near angular momentum compensation temperature, Nat. Commun. **9**, 4984 (2018).

[27] T. Kikkawa, M. Suzuki, R. Ramos, M. H. Aguirre, J. Okabayashi, K. Uchida, I. Lucas, A. Anadón, D. Kikuchi, P. A. Algarabel, L. Morellón, M. R. Ibarra, and E. Saitoh, Interfacial ferromagnetism and atomic structures in high-temperature grown $\mathrm{Fe_3O_4/Pt/Fe_3O_4}$ epitaxial trilayers, J. Appl. Phys. **126**, 143903 (2019).

[28] H. B. Vasili, M. Gamino, J. Ga, F. Sa, M. Valvidares, P. Gargiani, E. Pellegrin, and J. Fontcuberta Magnetoresistance in hybrid $\mathrm{Pt/CoFe_2O_4}$ bilayers controlled by competing spin accumulation and interfacial chemical reconstruction, ACS Appl. Mater. Interfaces **10**, 12031 (2018).

[29] C. Chappert, K. Le Dang, P. Beauvillain, H. Hurdequint, and D. Renard, Ferromagnetic resonance studies of very thin cobalt films on a gold substrate, Phys. Rev. B **34**, 3192 (1986).

[30] J. Lindner, I. Barsukov, C. Raeder, C. Hassel, O. Posth, R. Meckenstock, P. Landeros, and D. L. Mills, Two-magnon damping in thin films in case of canted magnetization: Theory versus experiment, Phys. Rev. B **80**, 224421 (2009).

[31] J. Dubowik, K. Załęski, H. Głowiński, and I. Gościańska, Angular dependence of ferromagnetic resonance linewidth in thin films, Phys. Rev. B **84**, 184438 (2011).

[32] Y. Fu, L. Sun, J. S. Wang, X. J. Bai, Z. X. Kou, Y. Zhai, J. Du, J. Wu, Y. B. Xu, H. X. Lu, and H. R. Zhai, Magnetic properties of $(\mathrm{Ni}_{83}\mathrm{Fe}_{17})_{1-x}\text{-}\mathrm{Gd}_x$ thin films with diluted Gd doping, IEEE Trans. Magn. **45**, 4004 (2009).

[33] S. Mizukami, Y. Ando, and T. Miyazaki, The study on ferromagnetic resonance linewidth for NM/NiFe/NM (NM = Cu, Ta, Pd and Pt) films, Jpn. J. Appl. Phys. **40**, 580 (2001).

[34] J. M. Shaw, H. T. Nembach, and T. J. Silva, Determination of spin pumping as a source of linewidth in sputtered $\mathrm{Co_{90}Fe_{10}/Pd}$ multilayers by use of broadband ferromagnetic resonance spectroscopy, Phys. Rev. B **85**, 054412 (2012).

[35] Y. Tserkovnyak, A. Brataas, and G. E. W. Bauer, Enhanced Gilbert Damping in Thin Ferromagnetic Films, Phys. Rev. Lett. **88**, 117601 (2002).

[36] M. Fang, Y. Wang, H. Wang, Y. Hou, E. Vetter, Y. Kou, W. Yang, L. Yin, Z. Xiao, Z. Li, L. Jiang, H. N. Lee, S. Zhang, and R. Wu, Tuning the interfacial spin-orbit coupling with ferroelectricity, Nat. Commun. **11**, 2627 (2020).

[37] B. Khodadadi, J. B. Mohammadi, C. Mewes, T. Mewes, M. Manno, C. Leighton, and C. W. Miller, Enhanced spin pumping near a magnetic ordering transition, Phys. Rev. B **96**, 054436 (2017).

[38] L. Frangou, S. Oyarzún, S. Auffret, L. Vila, S. Gambarelli, and V. Baltz, Enhanced Spin Pumping Efficiency in Antiferromagnetic IrMn Thin Films Around the Magnetic Phase Transition, Phys. Rev. Lett. **116**, 077203 (2016).